Applied Mathematical Modelling 39 (2015) 654–666

Contents lists available at ScienceDirect

Applied Mathematical Modelling

journal homepage: www.elsevier.com/locate/apm

A non-iterative mathematical description of three-dimensional bifurcation geometry for biofluid simulations

Guigao Le [a], Junfeng Zhang [b,*]

[a] School of Mechanical Engineering, Nanjing University of Science and Technology, Nanjing, Jiangsu 210094, China
[b] Bharti School of Engineering, Laurentian University, Sudbury, ON P3E 2C6, Canada

ARTICLE INFO

Article history:
Received 11 October 2013
Received in revised form 4 May 2014
Accepted 20 June 2014
Available online 9 July 2014

Keywords:
Lung airways
Bifurcation
Aerosol deposition
Biofluid
Numerical modeling
Computational fluid dynamics

ABSTRACT

We propose a mathematical model to describe the three-dimensional bifurcation geometry for airway flow simulations. The numerical scheme is explicit, non-iterative, and therefore stable and efficient. In addition, our model successfully reproduces the characteristic cross-sectional shape transition (from circular, to flattened elliptical, and then to 8-like shapes) across a bifurcation as observed in anatomical examinations. Several examples with various bifurcation parameters are presented, and these examples demonstrate the capacity and usefulness of our work in airway flow and transport simulations. The model developed here may also be useful for blood flow simulations and experimental model design.

1. Introduction

Bifurcations are the fundamental structure of the human and animal respiratory system, where an airway splits into two smaller daughter branches [1,2]. To investigate the complicated flow and transport processes in such bifurcation regions, numerical simulations have been proven to be useful [3–10]. Thanks to the advanced computational facilities and technologies, patient-specific calculations are possible with system geometry reconstructed from CT (Computed tomography) or MRI (magnetic resonance imaging) images [11,6,12,13]. However, information obtained from such simulations is limited to that particular situation. For general and fundamental studies aiming at a better understanding of the mechanisms and effects of various parameters on the flow and transport behaviors, an analytical description based on anatomical observations of these flow passages is more desirable [14]. While the straight segments between two consecutive bifurcations can be approximately considered as circular tubes, it is not a trivial task to construct a mathematical formulation for the three-dimensional (3D) bifurcation surface, which connects the parent and daughter branches smoothly.

Efforts in this direction can be traced back to the work by Gradon and Orlicki [15], where three types of rational functions were employed to describe a sequence of inter-penetrating cylindroids to construct the bifurcation geometry. In addition to the mathematical complexity, this model is limited to symmetric bifurcations, while asymmetric branching is very common in pulmonary architecture [2]. The *narrow* and *wide* models were then developed by Balashazy and Hofmann [16] to incorporate the branching asymmetry, where the carina is modeled as a sharp wedge and the side surfaces of the transition zone

* Corresponding author. Address: Bharti School of Engineering, Laurentian University, 935 Ramsey Lake Road, Sudbury, ON P3E 2C6, Canada. Tel.: +1 705 675 1151x2248; fax: +1 705 675 4862.
E-mail address: jzhang@laurentian.ca (J. Zhang).

http://dx.doi.org/10.1016/j.apm.2014.06.013
0307-904X/

Nomenclature

D_{DL}	diameter of the straight part of the left branch
D_{DR}	diameter of the straight part of the right branch
D_P	diameter of the parent airway
L_{DL}	length of the straight part of the left branch
L_{DR}	length of the straight part of the right branch
L_P	length of the parent airway
R_L	local tube radius along the left branch
R_L^*	curvature radius of the left branch
R_{LR}	local tube radius along the transition arc between two branches
R_{LR}^*	curvature radius of the transition arc between two branches
R_R	local tube radius along the right branch
R_R^*	curvature radius of the right branch
r_c	carinal curvature radius
s_L	curvilinear coordinate along the left branch axis
s_{LR}	curvilinear coordinate along the transition arc between two branches
s_R	curvilinear coordinate along the right branch axis
w_L	weight factor to the left branch axis
w_{LR}	weight factor to the transition arc between two branches
w_R	weight factor to the right branch axis
δ	cut-off value for the surface height calculation at central zone corners
ϵ	gradient transition function
ϵ'_0	spatial gradient of local tube radius at the intersection point of the left branch axis and the transition arc
ϵ'_1	spatial gradient of local tube radius at the intersection point of the right branch axis and the transition arc
σ	sigmoidal transition function
Φ_L	left branching angle
Φ_R	right branching angle
ϕ_L	left sagittal angle
ϕ_L^c	left sagittal angle where the branch diameter becomes constant
ϕ_L^*	left sagittal angle where the branch separates from the bifurcation
ϕ_{LR}	sagittal angle along the transition arc between two branches
ϕ_R	right sagittal angle
ϕ_R^c	right sagittal angle where the branch diameter becomes constant
ϕ_R^*	right sagittal angle where the branch separates from the bifurcation

are not smooth either. In 1995, Heistracher and Hofmann proposed to describe the carinal region with rounding circles to smoothly connect the two daughter branches [17]. As noticed later by Hegedus et al. [14], the mathematical descriptions in Ref. [17] were rather sketchy and the two-parameter iteration is numerically sensitive and hard to reproduce. They therefore improved this rounding-circle approach with more rigorous formulations for the carinal region, and the problematic two-parameter iteration was replaced by a one-parameter root-finding process. Even with this improvement, numerical instability may still be encountered in the carina rounding process, depending on the control geometric parameters and the transition functions utilized [14]. To avoid the numerical difficulty associated with the rounding-circle approach, which works in planes parallel to the bifurcation plane (the plane where the axes of the parent and daughter branches lie), Lee et al. [18] suggested to construct the bifurcation shape in the vertical cross-sections perpendicular to the bifurcation plane. In place of the iteration or root-finding process in the rounding-circle methods [17,14], a six-order polynomial fitting is necessary to smoothly connect the branch circular arcs across the bifurcation [18]. Such a high-order polynomial fitting is still iterative and sensitive to initial guess of the coefficients, and could be computationally unstable. A nonlinear equation also needs to be solved to determine the separating line (called the boundary curve there) location. Although this method might be attractive for highly asymmetric bifurcations, the symmetric bifurcation from this model has a deep indentation groove up to the very parental end (see Figs. 8a and 10a in Ref. [18]). This is different from the physiological observations, which indicate that the transition section consists of two regions: an elliptical region where the circular parent tube gradually changes to an elliptical shape with flattened top and bottom sides; and the carinal region where two indentations appear and grow in the middle of the top and bottom surfaces, leading to an 8-like cross-sectional shape and eventually two separate circles [2,19,17]. A similar problem also exists with the rounding-circle methods due to the non-zero rounding radius near the parental end.

In this paper, other than constructing the two-dimensional cross-sectional shapes in planes parallel [17,14] or perpendicular [18] to the bifurcation plane, we look the transition region as a 3D surface, and propose an explicit, robust, and non-iterative mathematical description for the bifurcation geometry. No iteration process of root-finding or nonlinear fitting is

involved and therefore this numerical scheme is efficient and stable. Symmetric and asymmetric examples will be presented and compared to those from previous models. At last, results of an example flow simulation will be provided to illustrate the practical usefulness of this model.

2. Model development

2.1. General description of bifurcation geometry

Heistracher and Hofmann had developed a simplified geometric description for airway bifurcations based on anatomical observations [17], and this geometric model has been adopted by later studies [14,18]. Here we follow this tradition and Fig. 1 displays the boundary outline in the bifurcation plane. The model starts with the parent tube modeled as a straight cylinder of length L_P and diameter D_P (the region between sections AA′ and BB′). It then gradually expends toward the left and right sides over the transition zone (the region bounded by sections AA′, CC′, and FF′), and finally two separate daughter branches are formed at sections CC′ and FF′, respectively. Further downstream from the transition region, each daughter branch continues as curved (segments between sections CC′ and DD′ or between FF′ and GG′) and then straight (segments

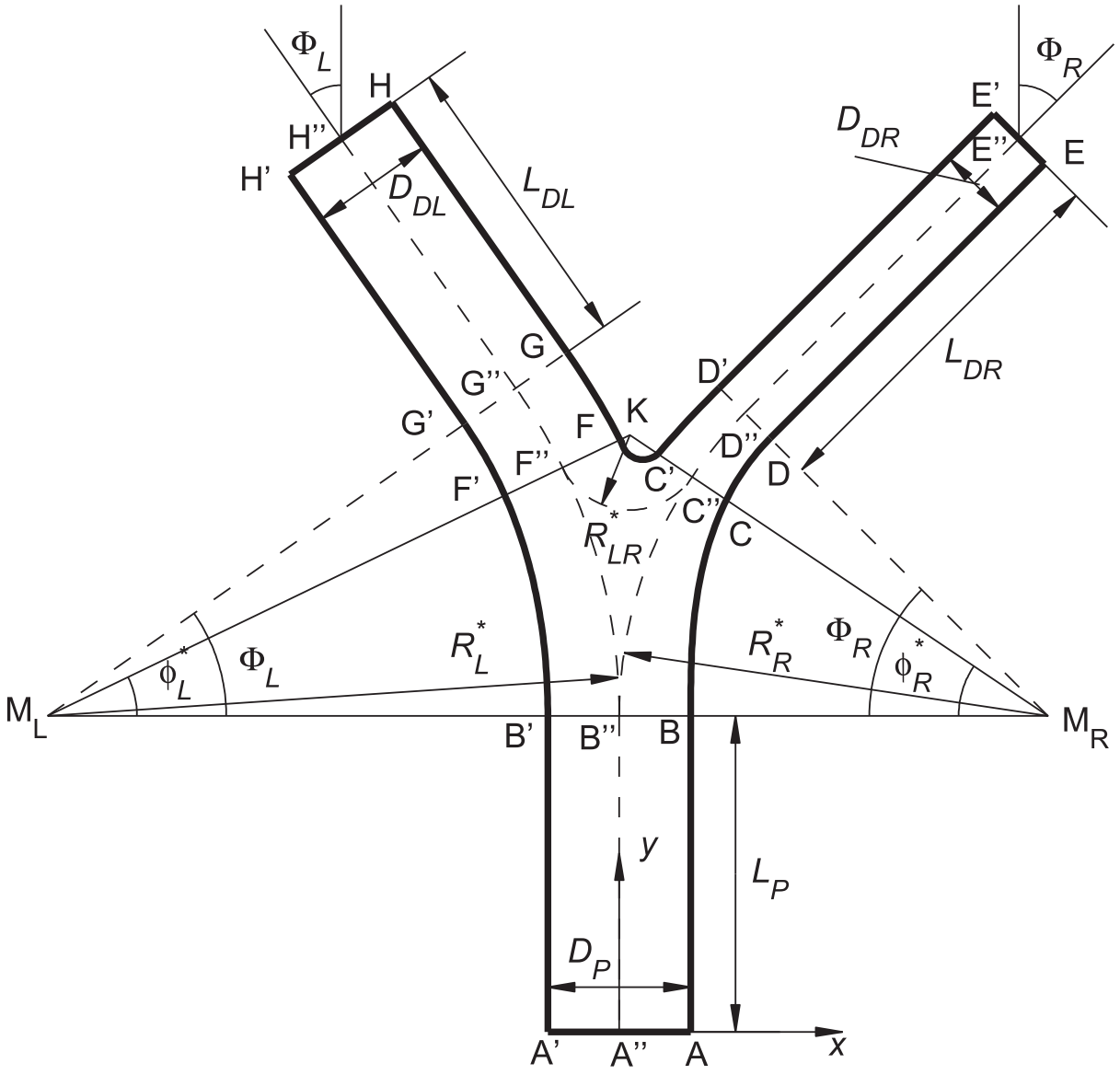

Fig. 1. The geometric structure of a general asymmetric bifurcation in the bifurcation plane. See details in text.

between sections DD′ and EE′ or between GG′ and HH′) segments. The daughter branch axes (dashed curves B″–C″–D″–E″ and B″–F″–G″–H″) are assumed to originate from the parental end at B″ and curve aside with respective radii (R_L^* for the left and R_R^* for the right branches) up to certain angles (Φ_L for the left and Φ_R for the right branches). These angles are equal to the respective branching angles (the orientation angles of the final straight branch tubes), as illustrated in Fig. 1. It is also usually assumed that the tube size reduces gradually along the curves part, and the straight segment has a constant diameter, D_{DL} for the left and D_{DR} for the right branches [17,14]. In another words, the sagittal angles (ϕ_L^c and ϕ_R^c) where the branch radii become constant are assumed to be the same as the respective branching angles (i.e., $\phi_L^c = \Phi_L$ and $\phi_R^c = \Phi_R$), although the model description below can be readily extended to more general situations with $\phi_L^c < \Phi_L$ and $\phi_R^c < \Phi_R$. The lengths of the straight segments of daughter branches are denoted by L_{DL} and L_{DR}, respectively.

2.2. Surface height calculation

In this work, we limit our discussions to a bifurcation symmetric about its axis plane, although the left and right branching angles and diameters could be different. Due to this plane symmetry, for a certain point in the bifurcation plane, there are two corresponding surface points: one above and one below the bifurcation plane, and the distances to the plane are the same. For this reason, here we only talk about the upper half of the bifurcation surface, and the lower half is just an image of the upper one. We set our Cartesian coordinate system with the x–y plane in the bifurcation plane and the origin at A″ (Fig. 1). Axis y follows the parent tube axis, and axis x directs toward the right side. The z axis is then perpendicular to and pointing outward of the bifurcation plane. For our convenience of discussion, we will separate the bifurcation structure into nine parts, and equations will be provided for points in each part to calculate the surface height z from a given pair of x and y.

(1) *The parent tube* (Region between sections AA′ and BB′).

This straight segment is circular and the diameter is constant, and therefore the z-coordinate can be readily calculated by

$$z = \sqrt{D_P^2/4 - x^2}, \tag{1}$$

and the application of this equation is limited to the range of $-D_P/2 \leqslant x \leqslant D_P/2$ and $0 \leqslant y \leqslant L_P$.

(2) *The left side surface of the transition zone* (Region delimited by B′B″, B″F″, F″F′, and F′B′).

As in previous modes [17,14,18], this portion of the surface is considered as circular with variational radius $R_L(\phi_L)$ along the curved axis B″F″. Here ϕ_L is the left sagittal angle of the current location (x, y) relative to the left branch curvature center M_L, and it can be obtained by

$$\phi_L = \tan^{-1}\left(\frac{y - L_p}{R_L^* + x}\right). \tag{2}$$

To have a smooth transition in radius along the branch axis, a sigmoidal function σ is typically employed [17,14,18]. In principle, this function σ should vary monotonously and smoothly from one value to another over a certain interval, and its first-order derivative should disappear as approaching the interval ends. Several choices, such as a shifted-and-scaled sine or cosine function or the smooth Heaviside function [20], are available; however, here we follow previous studies [17,14,18] and adopt the following transition function:

$$\sigma(t) = -2t^3 + 3t^2, \quad 0 \leqslant t \leqslant 1. \tag{3}$$

The local tube radius $R_L(\phi_L)$ can then be obtained via

$$R_L(\phi_L) = D_P/2 + (D_{DL}/2 - D_P/2)\sigma(\phi_L/\phi_L^c). \tag{4}$$

Here ϕ_L^c is the sagittal angle where the left branch has achieved its constant diameter D_{DL}. As in previous studies [17,14], we use $\phi_L^c = \Phi_L$ in this work.

The surface height above a point (x, y) in this region is then given be

$$z = \sqrt{R_L^2(\phi_L) - \left[R_L^* - \sqrt{(R_L^* + x)^2 + (y - L_p)^2}\right]^2}. \tag{5}$$

In this region, we have $0 \leqslant \phi_L \leqslant \phi_L^*$ (ϕ_L^* is the sagittal angle at section FF′ where the left daughter branch separates from the bifurcation. This angle is determined below in Eq. 15) and $R_L^* - R_L(\phi_L) \leqslant \sqrt{(R_L^* + x)^2 + (y - L_P)^2} \leqslant R_L^*$ (the outside part of the ring).

(3) *The curved segment of the left branch* (Region between sections FF′ and GG′).

Eqs. (2)–(5) are still applicable in this region; and the only difference is that here we have the entire circular tube surface $R_L^* - R_L(\phi_L) \leqslant \sqrt{(R_L^* + x)^2 + (y - L_P)^2} \leqslant R_L^* + R_L(\phi_L)$ with the sagittal angle in the range of $\phi_L^* \leqslant \phi_L \leqslant \Phi_L$ (Φ_L is the sagittal angle at section GG′ where the left daughter branch becomes straight).

(4) *The straight segment of the left branch* (Region between sections GG′ and HH′).

This part of the daughter branch is a straight cylinder with a constant diameter D_{DL} and an inclination angle Φ_L. The z-coordinate on the surface for a given point (x, y) can then be calculated from the distance from this point to the left branch centerline G″H″ by

$$z = \sqrt{D_{DL}^2/4 - (x\cos\Phi_L + y\sin\Phi_L - x_{G''}\cos\Phi_L - y_{G''}\sin\Phi_L)^2}, \tag{6}$$

where $(x_{G''}, y_{G''})$ is the location of point G″ in the bifurcation plane:

$$x_{G''} = R_L^*(\cos\Phi_L - 1), \quad y_{G''} = L_P + R_L^*\sin\Phi_L. \tag{7}$$

(5) *The right side surface of the transition zone* (Region delimited by BB″, B″C″, C″C, and CB).

The treatment on this region is very similar to that for the left side surface described above, and hence here we just give the corresponding equations as:

Right sagittal angle:

$$\phi_R = \tan^{-1}\left(\frac{y - L_p}{R_R^* - x}\right); \tag{8}$$

Local radius:

$$R_R(\phi_R) = D_P/2 + (D_{DR}/2 - D_P/2)\sigma(\phi_R/\phi_R^c); \tag{9}$$

Surface height:

$$z = \sqrt{R_R^2(\phi_R) - \left[R_R^* - \sqrt{(R_R^* - x)^2 + (y - L_p)^2}\right]^2}. \tag{10}$$

Also we use $\phi_R^c = \Phi_R$ for simplicity.

(6) *The curved segment of the right branch* (Region between sections CC′ and DD′).

Again here we can still use Eqs. (8)–(10), but for the entire circular surface between angles ϕ_R^* and Φ_R.

(7) *The straight segment of the right branch* (Range between sections DD′ and EE′).

For this segment, Eqs. (6) and (7) have been slightly modified as:

$$z = \sqrt{D_{DR}^2/4 - (x\cos\Phi_R - y\sin\Phi_R - x_{D''}\cos\Phi_R + y_{D''}\sin\Phi_R)^2}; \tag{11}$$

$$x_{D''} = R_R^*(1 - \cos\Phi_R), \quad y_{D''} = L_P + R_R^*\sin\Phi_R. \tag{12}$$

(8) *The carinal transition region between daughter branches* (Region bounded by FF″, F″C″, C″C′, and C′F).

So far the modeling and treatments for the above mentioned parts are identical to those in previous methods [17,14,18]. The key differences in our present model from existing ones lie in the treatments for the last two regions, and we discuss the carinal transition ring region here first. To smoothly connect the right half of the left branch end (section FF″) to the left half of the right branch end (section C′C″), we propose to employ a similar approach as we do with the left and right side surfaces. For this purpose, we introduce the transition radius R_{LR}^* (Fig. 1). With R_{LR}^* available, the transition curvature center K can be determined as the third vertex of a triangle $\triangle KM_LM_R$ such that $|KM_L| = R_L^* + R_{LR}^*$ and $|KM_R| = R_R^* + R_{LR}^*$ (Fig. 1). Here the absolute signs are adopted to represent the distances between pairs of points in the bifurcation plane. The coordinates of point K can be calculated out explicitly as

$$x_K = -R_L^* + (R_L^* + R_{LR}^*)\cos\phi_L^*, \quad y_K = L_P + (R_L^* + R_{LR}^*)\sin\phi_L^*; \tag{13}$$

or

$$x_K = R_R^* - (R_R^* + R_{LR}^*)\cos\phi_R^*, \quad y_K = L_P + (R_R^* + R_{LR}^*)\sin\phi_R^*; \tag{14}$$

with the branch end angles given by

$$\cos\phi_L^* = \frac{(R_L^* + R_{RL}^*)^2 + (R_L^* + R_R^*)^2 - (R_R^* + R_{RL}^*)^2}{2(R_L^* + R_{RL}^*)(R_L^* + R_R^*)}; \tag{15}$$

$$\cos\phi_R^* = \frac{(R_R^* + R_{RL}^*)^2 + (R_L^* + R_R^*)^2 - (R_L^* + R_{RL}^*)^2}{2(R_R^* + R_{RL}^*)(R_L^* + R_R^*)}, \tag{16}$$

according to the cosine law. With ϕ_L^* and ϕ_R^* calculated from Eqs. (15) and (16), Eqs. (13) and (14) actually yield the same coordinates for point K.

At section FF′ the left branch has a radius $R_L(\phi_L^*)$. Similarly, at section CC′ the radius of the right branch end is $R_R(\phi_R^*)$. However, we cannot simply use the transition function σ Eq. (3) to calculate the intermediate local radius along the transition arc F″C″ as we do with side branches, since the σ function has zero first-order derivatives at the interval ends, while there may

be non-zero radius gradients at points F″ (if $\phi_L^* \neq \phi_L^c$) and/or C″ (if $\phi_R^* \neq \phi_R^c$). Otherwise sharp edges will be resulted in, and the surface will not be smooth at cross-sections FF″ and C″C′. To avoid such defects, we introduce the following gradient transition function ϵ:

$$\epsilon(\epsilon_0', \epsilon_1', t) = (\epsilon_0' + \epsilon_1')t^3 - (2\epsilon_0' + \epsilon_1')t^2 + \epsilon_0' t, \quad 0 \leqslant t \leqslant 1. \tag{17}$$

It can be shown that this function has zero function values at $t = 0$ and $t = 1$, and it has the desired first-order derivatives ϵ_0' at $t = 0$ and ϵ_1' at $t = 1$.

To have a smooth transition in local radius at point F″, we need to set the spatial gradient of local radius in the direction leaving F″ along the transition arc F″C″ to be the same as that in the direction approaching F″ from G″F″ along the left branch axis; and a similar statement applies to the situation at point C″. For convenience, we define three one-dimensional curvilinear coordinates along these arcs: s_L along the left branch axis from G″ to B″; s_R along the right branch axis from B″ to D″; and s_{LR} along the transition arc from F″ to C″ (Fig. 2). The smooth transition requirement in radius gradient is then expressed as:

$$\left.\frac{dR_L(\phi_L)}{ds_L}\right|_{\phi_L=\phi_L^*} = \left.\frac{dR_{LR}(\phi_{LR})}{ds_{LR}}\right|_{\phi_{LR}=0}; \tag{18}$$

$$\left.\frac{dR_R(\phi_R)}{ds_R}\right|_{\phi_R=\phi_R^*} = \left.\frac{dR_{LR}(\phi_{LR})}{ds_{LR}}\right|_{\phi_{LR}=\pi-\phi_L^*-\phi_R^*}. \tag{19}$$

The transition angle ϕ_{LR} measures from line KF″ up to KC″ and its value can be obtained from the x and y coordinates of a point in this region as

$$\phi_{LR} = \frac{\pi}{2} - \phi_L^* + \tan^{-1}\left(\frac{x - x_K}{y_K - y}\right). \tag{20}$$

Recall that the local radii $R_L(\phi_L)$ and $R_R(\phi_R)$ are calculated from Eqs. (4) and (9) via the sigmoidal function Eq. (3), we then have

$$\left.\frac{dR_L(\phi_L)}{ds_L}\right|_{\phi_L=\phi_L^*} = -\frac{D_{DL} - D_P}{2R_L^*\phi_L^c}\left.\frac{\sigma}{dt}\right|_{t=\phi_L^*/\phi_L^c}; \tag{21}$$

$$\left.\frac{dR_R(\phi_R)}{ds_R}\right|_{\phi_R=\phi_R^*} = \frac{D_{DR} - D_P}{2R_R^*\phi_R^c}\left.\frac{\sigma}{dt}\right|_{t=\phi_R^*/\phi_R^c}. \tag{22}$$

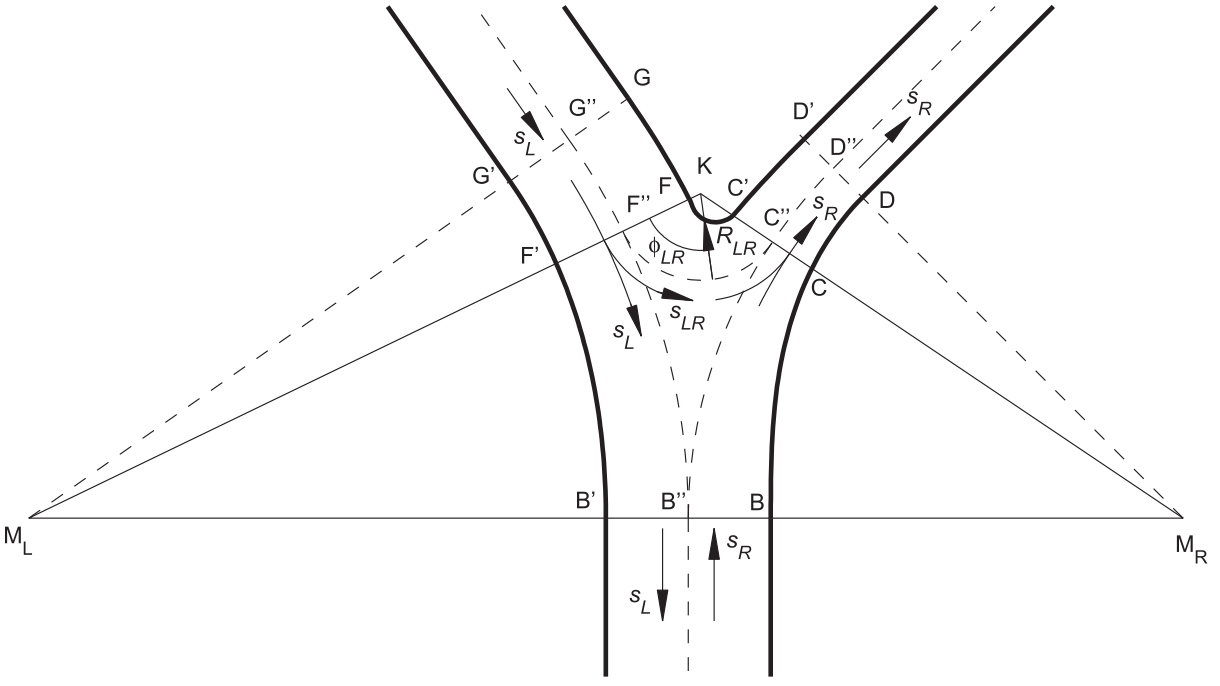

Fig. 2. The carinal transition region and the curvilinear coordinate systems.

The negative sign in Eq. (21) comes from the fact that the sagittal angle ϕ_R increases in the opposite direction of s_L. Putting these equations together, we now can write the local radius along the transition arc F″C″ as

$$R_{LR}(\phi_{LR}) = R_L(\phi_L^*) + [R_R(\phi_R^*) - R_L(\phi_L^*)]\sigma\left(\frac{\phi_{LR}}{\pi - \phi_L^* - \phi_L^*}\right) + R_{LR}^*\epsilon\left(\epsilon_0', \epsilon_1', \frac{\phi_{LR}}{\pi - \phi_L^* - \phi_L^*}\right), \tag{23}$$

where

$$\epsilon_0' = -\frac{(D_{DL} - D_P)R_{LR}^*(\pi - \phi_L^* - \phi_R^*)}{2R_L^*\phi_L^c}\left.\frac{d\sigma}{dt}\right|_{t=\phi_L^*/\phi_L^c}; \tag{24}$$

$$\epsilon_1' = \frac{(D_{DR} - D_P)R_{LR}^*(\pi - \phi_L^* - \phi_R^*)}{2R_R^*\phi_R^c}\left.\frac{d\sigma}{dt}\right|_{t=\phi_R^*/\phi_R^c}; \tag{25}$$

and the derivative of σ is readily available from Eq. (3)

$$\frac{d\sigma}{dt} = -6t^2 + 6t, \quad 0 \leqslant t \leqslant 1. \tag{26}$$

Once the local radius $R_{LR}(\phi_{LR})$ is obtained, the surface height can be found in a similar fashion as in other regions:

$$z = \sqrt{R_{LR}^2(\phi_{LR}) - \left[R_{LR}^* - \sqrt{(x - x_K)^2 + (y - y_K)^2}\right]^2}. \tag{27}$$

For this current carinal region, we should have $0 \leqslant \phi_{LR} \leqslant \pi - \phi_L^* - \phi_R^*$ and $R_{LR}^* - R_{LR}(\phi_{LR}) \leqslant \sqrt{(x - x_K)^2 + (y - y_K)^2} \leqslant R_{LR}^*$.

(9) *The central region* (Region enclosed by arcs B″C″, C″F″, and F″B″).

The last part that we have not discussed by now is the central region of the transition zone, and we would call it the circular triangle B″C″F″. The current situation is that we have the surface height (z-coordinate) values all defined on its three circular edges, and we need to find a way to construct a 3D surface patch which meets each circular edge (including the vertices B″, C″, and F″) smoothly.

Consider a point P (x, y) in the central region as shown in Fig. 3. We connect this point to the three arc centers (M_L, M_R and K), and the lines intersects with the edges at, respectively, P_L, P_R and P_{LR}. From the corresponding arc angles ϕ_L, ϕ_R and ϕ_{LR}, we can have the surface heights at these intersection points, which are $R_L(\phi_L), R_R(\phi_R)$, and $R_{LR}(\phi_{LR})$, respectively. In addition, three weight factors are defined to measure how close this interesting point P is to each circular edge:

$$w_L = \frac{|M_LP| - R_L^*}{|M_LC''| - R_L^*}, \quad w_R = \frac{|M_RP| - R_R^*}{|M_RF''| - R_R^*}, \quad w_{LR} = \frac{|KP| - R_{LR}^*}{|KB''| - R_{LR}^*}. \tag{28}$$

One can see that we will have $w_L = 0$ on the edge B″F″ and $w_L = 1$ at the vertex C″.

We then propose the following equation to calculate the surface height above point P as:

$$z = \frac{(1 - w_L)w_Rw_{LR}R_L(\phi_L) + w_L(1 - w_R)w_{LR}R_R(\phi_R) + w_Lw_R(1 - w_{LR})R_{LR}(\phi_{LR})}{(1 - w_L)w_Rw_{LR} + w_L(1 - w_R)w_{LR} + w_Lw_R(1 - w_{LR})}. \tag{29}$$

This particular equation is constructed such that the calculated z value approaches the edge value as point P moves toward an edge. At the vertices, a 0/0 singularity exists. Although the mathematical limit of this singularity is the correct corner height value, computer calculations may break down in the very close vicinities of the vertices. To avoid such possible interruptions, in computer program we can include the following treatments:

$$z = D_P/2, \quad \text{if } w_L \leqslant \delta \quad \text{and} \quad w_R \leqslant \delta; \tag{30}$$

$$z = R_L(\phi_L^*), \quad \text{if } w_L \leqslant \delta \quad \text{and} \quad w_{LR} \leqslant \delta; \tag{31}$$

$$z = R_R(\phi_R^*), \quad \text{if } w_R \leqslant \delta \quad \text{and} \quad w_{LR} \leqslant \delta; \tag{32}$$

where δ is a very small quantity as a resolution control parameter. In our calculations, we use $\delta = 10^{-6}$ mm.

2.3. Input control parameters

For convenience to potential users of this model, here we summarize the input parameters required to define the bifurcation structure:

- diameters of the straight segments of the parent and daughter tubes (D_P, D_{DL}, D_{DR});
- branching angles of the daughter tubes (Φ_L, Φ_R);
- curvature radii of the daughter tubes (R_L^*, R_R^*); and
- curvature radius of the carinal connection (R_{RL}^*).

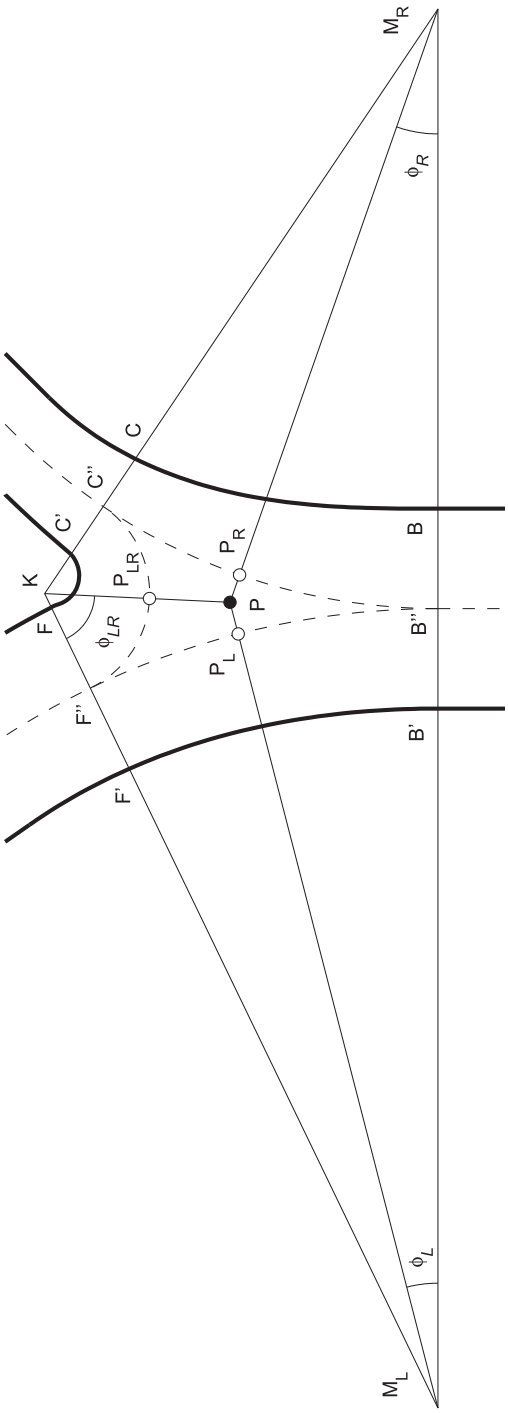

Fig. 3. The central circular triangular region and the intersection points.

Unlike previous models [17,14,18], the carinal rounding radius r_c is not involved in our present model, although it has been adopted in physiological airway characterization [2]. Actually, for general asymmetric bifurcations with unequal branch diameters, branching angles, and/or branching curvature radii, the carinal rounding radius might not be the best choice for the local geometry description. A rounding radius always implies a local left–right symmetry about the line passing the rounding center along the y-direction; and such a local symmetry should not be always expected for highly

asymmetric bifurcations. Nevertheless, for symmetric or slightly asymmetric bifurcations, if we neglect the further decrease in diameter after the branch ends [$R_L(\phi_L^*) \approx D_{DL}/2$ and $R_R(\phi_R^*) \approx D_{DR}/2$] and the radius gradients there, the transition arc radius R_{LR}^* can then be approximately related to the rounding radius r_c by

$$R_{LR}^* \approx (D_{DL} + D_{DR})/2 + r_c. \tag{33}$$

In addition to these geometric parameters, as mentioned in Ref. [14], different transition functions σ and ϵ (even different σ functions for the left/right or upper/lower sides of the bifurcation surface) can also be experimented to introduce more degrees of freedom for best descriptions of particular bifurcation structures. The lengths of the straight segments of the parent and daughter tubes (L_P, L_{DL}, and L_{DR}) are not considered as control parameters here, since they are not directly relevant to the bifurcation geometry. For some parameter combinations (e.g., a small branching angle with a short curvature radius on one same side), the calculated branch end angle (ϕ_L^* or ϕ_R^*) may be larger than the branching angle. In such situations, the mathematical relations in this paper need to be re-formulated by following the key ideas here, and this is a straightforward task.

3. Results and discussion

We have tested our method with different parameters and found that the method is stable and robust as long as the geometric relationships illustrated in Fig. 1 valid. Fig. 4 shows two bifurcations (one symmetric and one asymmetric) generated from our model. The control parameters (see figure caption) are taken from a previous study [14] for comparison. For a more careful examination, we then plot cross-sectional cuts in several constant-x and constant-y planes (Fig. 5). Again we see all these shape profiles are smoothly continuous. For the symmetric bifurcation along the y-direction (Fig. 5(a)), the cross-sectional shapes gradually change from a circle ($y = 3$ mm and $y = 4$ mm), an apparent ellipse ($y = 5$ mm), to a blunt shape with flattened top and bottom ($y = 6$ mm). After this location, the cross-sectional shape becomes indented inward on top and bottom, resembling the digit 8, and the indentation becomes more and more significant over a short distance ($y = 6.3$ mm to $y = 6.65$ mm). Finally, the top and bottom indentation points merge together ($y = 6.68$ mm), and two separate daughter branches are formed ($y = 7$ mm and $y = 8$ mm). This transition in cross-sectional shape is very similar to experimental observations [2,19]. Compared to those from a previous model [18], our model has successfully captured the elliptical/flat section in the transition zone, while the previous model produced an unrealistic indentation groove immediately after the parent tube end. Similar problems may also exist with the rounding-circle methods [17,14], due to the non-zero rounding-off radius [$r_c(z)$ there] along the entire carinal ridge (except the vey parental end point B″).

Fig. 5(b) displays the constant-x cuts from the symmetric line $x = 0$ to $x = 3$, where the right branch has completely developed. Again all the profiles are smooth and continuous in a reasonable fashion. The cord depth of the flow divider (see Fig. 14D in Ref. [2]) at $x = 0$ plane is found to be 5.4 mm, which is 0.77 times of the daughter branch diameter (7 mm). This agrees qualitatively with the physiological observations by Horsfield et al. [2], where they reported that the cord depth is approximately equal to or less than the branch diameter.

Such cross-sectional shapes of the asymmetric bifurcation are also plotted Fig. 5(c) and (d). The structure asymmetry is clear, and again all shapes are reasonable and smooth. Lee et al. [18] had pointed out that a distortion might be generated on the thinner-branch side for asymmetric bifurcations when the carinal ridge is forced to start at the parent tube center B″. No such distortion is observed in the bifurcation outline and the cross-sectional cuts in Fig. 5(d).

Different from previous models trying to connect the two branch surfaces in planes parallel or perpendicular to the bifurcation plane, here we use a transition arc F″C″. To verify the local radius change along the transition arc, in Fig. 6 we plot the variations of local radii R_L, R_R, and R_{LR} along their individual curvilinear coordinates s_L, s_R, and s_{LR}. For clarity, key positions along these paths, including points B″, C″, D″, F″, and G″, are also indicated as circles with labels. Curve $R_{LR} \sim s_{LR}$ separates from curve $R_L \sim s_L$ at the splitting point F″, and later merges to curve $R_R \sim s_R$ at the converging point C″. The change in R_{LR} at these two end points, as well as over the whole s_{LR}-region, is continuous and smooth for both symmetric and asymmetric cases, indicating that the gradient transition function ϵ and the relevant mathematical treatments work well for our purpose.

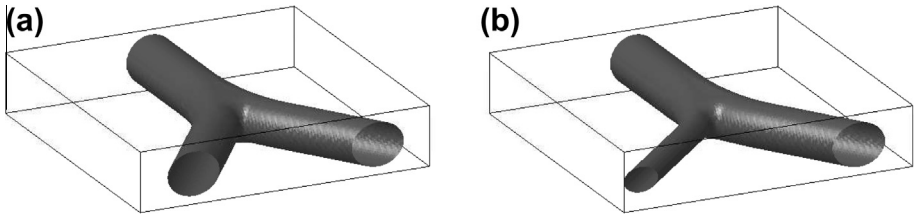

Fig. 4. The 3D shapes of a symmetric (a) ($D_P = 16$ mm, $D_{DL} = D_{DR} = 14$ mm, $\Phi_L = \Phi_R = 35^\circ$, $R_L^* = R_R^* = 64$ mm, $R_{LR}^* = 8$ mm) and an asymmetric (b) ($D_P = 16$ mm, $D_{DL} = 14$ mm, $D_{DR} = 8$ mm, $\Phi_L = 35^\circ, \Phi_R = 45^\circ$, $R_L^* = 64$ mm, $R_R^* = 48$ mm, $R_{LR}^* = 8$ mm) bifurcations.

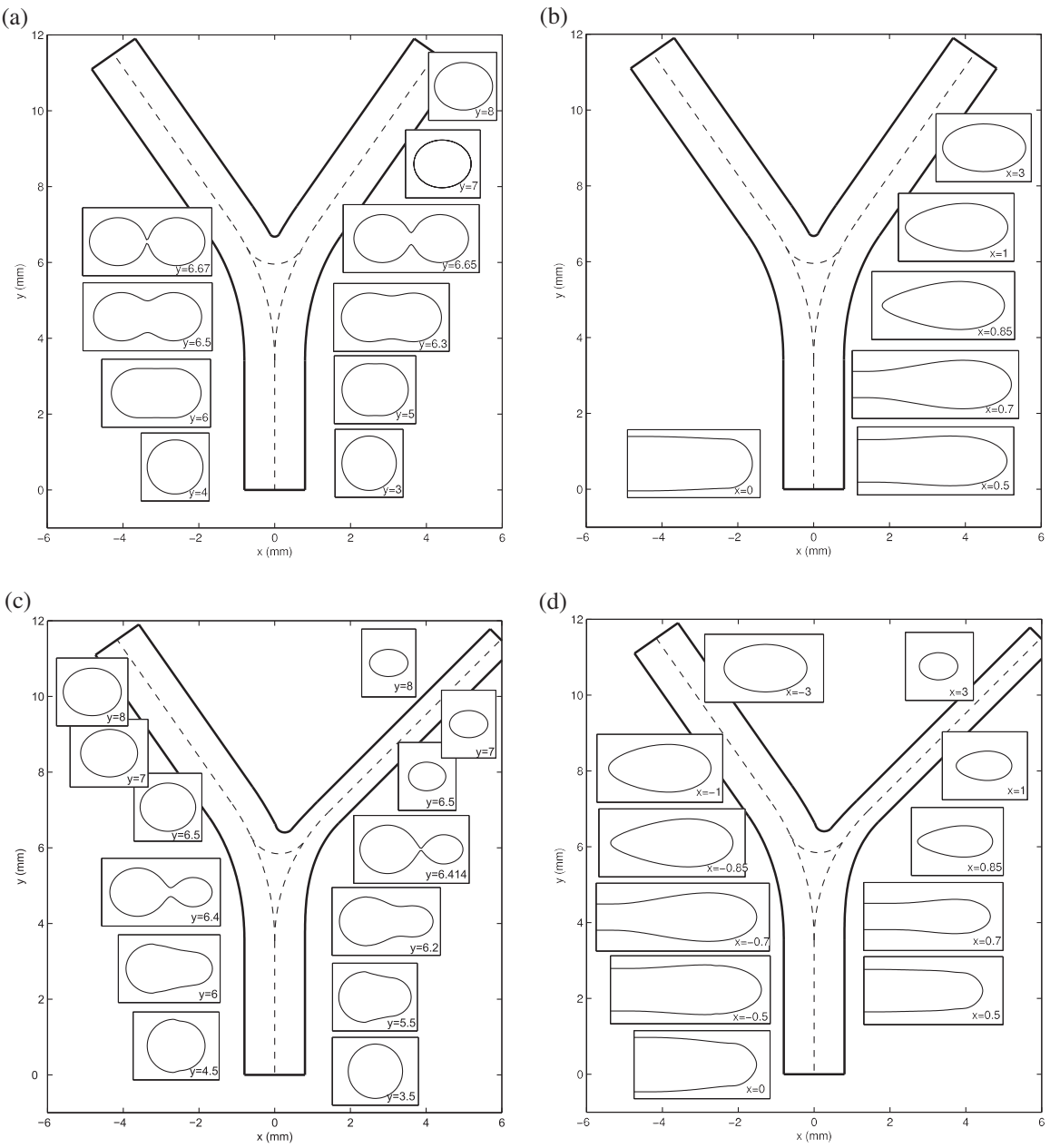

Fig. 5. The cross-section shapes of the symmetric (a and b) and asymmetric (c and d) bifurcations shown in Fig. 4 at different constant-y (top) and constant-x (bottom) locations.

To further explore the capacity of this model, four more asymmetric bifurcations are shown in Fig. 7, and the control parameters are listed in Table 1. These parameter combinations, although artificial, cover wide ranges of parent/daughter diameter ratio, branching angle, and curvature radius based on anatomical results [2,19]. As can be seen there, the surfaces in the transition zones are smooth and the parent and daughter branches are connected to the transition zones naturally. We also find that our method is stable and robust in all these systems, and therefore it is capable to model bifurcations with large differences in tube diameters, branching angles, and branching curvatures.

At last, we present an example flow simulation with the asymmetric bifurcation in Fig. 4(b) to illustrate the practical application of this model. A finite-volume computational fluid dynamics (CFD) program is utilized, with a parabolic velocity distribution with a maximum velocity U_m at the center applied at the parental end and a constant pressure at the two distal branch ends. In addition, linear variations for pressure at the inlet and velocity at the exits are assumed. These boundary conditions may not describe the actual airflows in airway trees well, and multiple-level bifurcations would be desirable

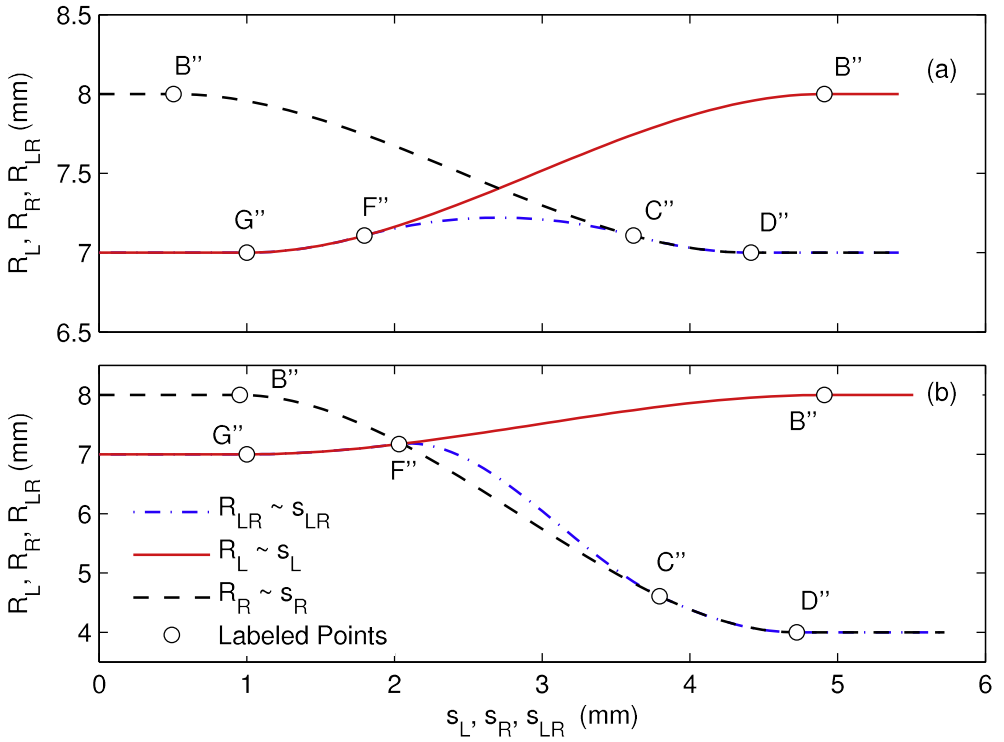

Fig. 6. The variations of local radii along the branch axes and transition arc for the symmetric (a) and asymmetric (b) bifurcations in Fig. 4.

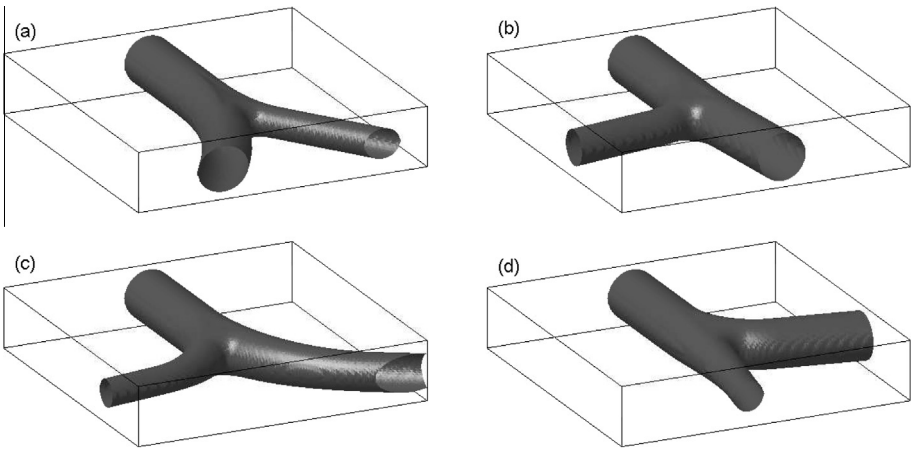

Fig. 7. The 3D shapes of more general asymmetric bifurcations. The control parameters to generate these structures are listed in Table 1.

[9,10]. Nevertheless, the simulation here is just an example and we are not aiming to examine any particular phenomena. The Reynolds number $Re = \rho U D_P/\mu$ (ρ is the fluid density, μ is the fluid viscosity, and $U = U_m/2$ is the mean flow velocity in the parent tube) is 1633, which is in the typical range for flows in the primary bronchi with similar diameters [19]. Fig. 8(a) displays the flow field in the bifurcation plane, with background colors for the velocity strength (normalized by the maximum inlet velocity $U_m = 2U$) and arrows for the flow direction. In the parent segment, the velocity profile is approximately parabolic, consistent to the fluid mechanics theory for laminar tube flows. The flow separates in the bifurcation region, and the higher flow rate into the left branch is due to its larger diameter and then the less flow resistance under a same pressure difference. Immediately after the bifurcation region, the flow velocity increases in both branches because of the no-slip boundary condition and mass conservation constraint. A low-flow region is also noticed near the right bifurcation wall, and this can be attributed to the lower flow rate into the narrower right branch and the relatively large branching angle there ($\phi_R = 45^o$). We have also examined the secondary flow patterns in several transverse cross-sectional

Table 1
Control parameters for the bifurcations shown in Fig. 7. The letters in the first column indicate the corresponding subfigure labels in Fig. 7.

	D_P (mm)	D_{DL} (mm)	D_{DR} (mm)	Φ_L (deg.)	Φ_R (deg.)	R_L^* (mm)	R_R^* (mm)	R_{LR}^* (mm)
(a)	20	18	12	30	35	150	80	11
(b)	20	14	19	80	6	30	350	12
(c)	20	11	15	80	80	45	80	10
(d)	20	12	19	10	10	400	30	12

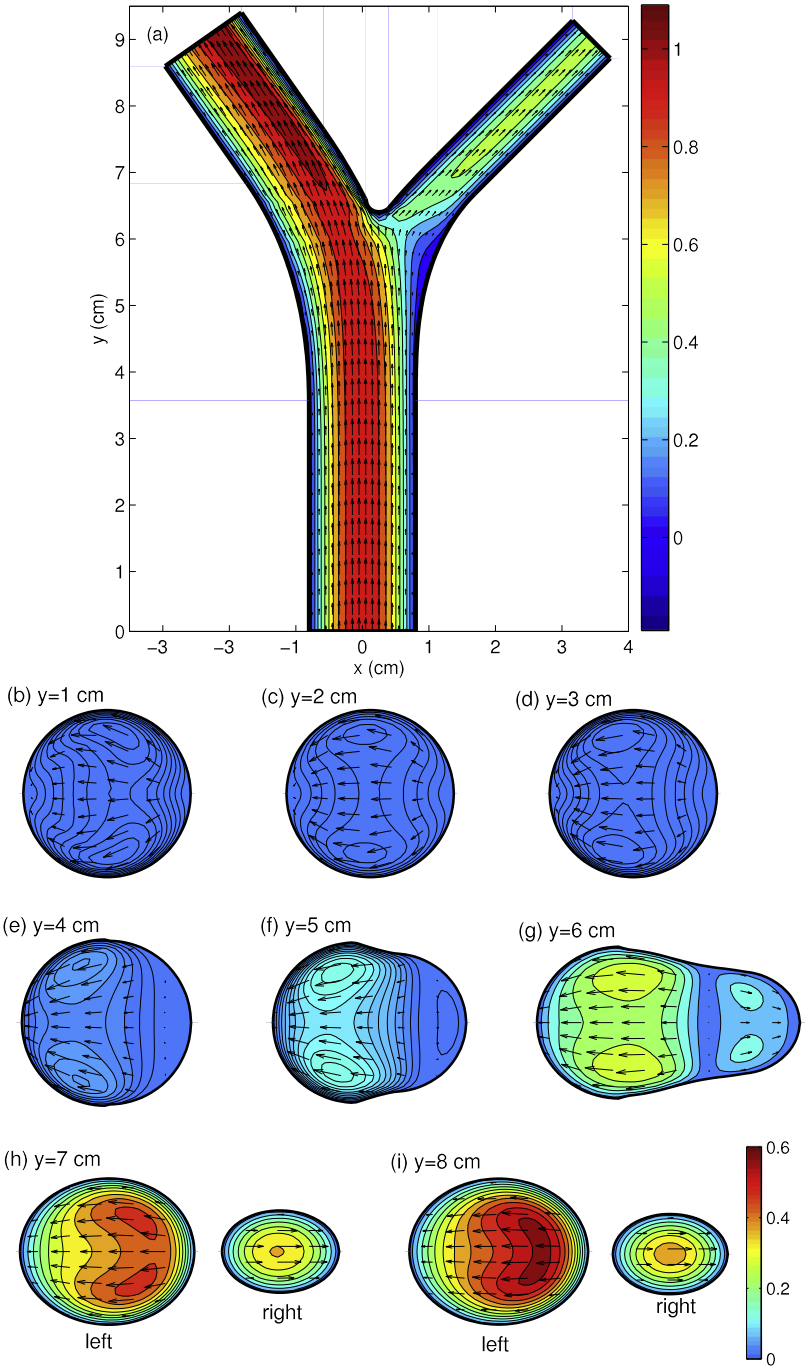

Fig. 8. The flow patterns in the bifurcation plane (a) and several transverse cross-sections (b-i). The background colors indicate the velocity magnitudes (normalized by the maximum inlet velocity U_m) and the arrows show the flow directions.

planes along the flow direction (Fig. 8(b)–(i)). Before $y = 3$ cm (Fig. 8(b)–(d)), we see no significant secondary flows, meaning that the flow here is mainly a tube flow in the axial direction. The maximum velocity magnitudes for the secondary flows there are $9.75 \times 10^{-5} U_m$ at $y = 1$ cm, $6.40 \times 10^{-4} U_m$ at $y = 2$ cm, and $4.50 \times 10^{-3} U_m$ at $y = 3$ cm. This secondary flow is flowing from the right to left, indicating that the mainstream flow is bending toward right to provide a high-flow-rate supply to the right branch, as can be seen in Fig. 8(a). The secondary flow strength increases as approaching the bifurcation region, and the maximum velocity grows up to $0.116 U_m$ at $y = 5$ cm (Fig. 8(f)). Meanwhile, a weaker and smaller left-to-right secondary flow pattern also gradually develops for the low-flow-rate right branch (Fig. 8(e)–(g)). The secondary flow patterns are all symmetric about the bifurcation plane at $z = 0$, and two high-flow regions (one above and one below the bifurcation plane) are observed for, respectively, the right-to-left and the left-to-right secondary flow patterns (Fig. 8(g)). After the flow has completely separated into two branches, the high-flow regions merge together, and the flow in each branch gradually adjusts toward the tube-flow situation (Fig. 8(h) and (i)). The flow in the narrower right branch has almost developed at the right exit, while the flow in the left branch is still highly asymmetric at the left exit (Fig. 8(a) and (i)), because a stronger flow in a wider tube requires a longer entrance length. Since this simulation is carried out with our new bifurcation model, a direct comparison with previous simulation results is not possible. Nevertheless, the above observations quantitatively agree with fluid mechanics theory and previous simulations [9,10,5].

4. Summary

We have developed an explicit and non-iterative mathematical model for the 3D geometry of airway bifurcations. The transition zone is separated into three half-ring segments at the edges and a central circular triangular region, and the surface height in the central zone is determined by a distance-to-edge weighted scheme. Compared to other existing methods, there is no iteration processes involved in our model, and therefore the numerical calculation is explicit and stable. Examples with various geometric control parameters are presented. More important, the typical cross-sectional shape change (from circular, to flattened elliptical, and to 8-like shapes) observed in anatomical studies has been successfully reproduced. Simulation results of a flow through an asymmetric bifurcation have also been presented to illustrate the potential model applications. This work may also be useful for blood flow simulations [21,22] and experimental model design [23].

Acknowledgments

This work has been supported by the National Natural Science Foundation of China (Grant No. 51303081), the Natural Science Foundation of Jiangsu Province (Grant No. BK20130761), the Natural Science and Engineering Research Council of Canada (NSERC), and the Laurentian University Research Fund (LURF).

Appendix A. Supplementary data

Supplementary data associated with this article can be found, in the online version, at http://dx.doi.org/10.1016/j.apm.2014.06.013.

References

[1] A. Davies, C. Moores, The Respiratory System: Basic Science and Clinical Conditions, Churchill Livingstone, 2010.
[2] K. Horsfield, G. Dart, D.E. Olson, G.F. Filley, G. Cumming, J. Appl. Physiol. 31 (1971) 207.
[3] W. Hofmann, J. Aerosol Sci. 42 (2011) 693.
[4] R.C. Martinez, A. Roshchenko, P. Minev, W.H. Finlay, J. Aerosol Med. Pulmonary Drug Delivery 26 (2013) 31.
[5] M. Pilou, V. Antonopoulos, E. Makris, P. Neofytou, S. Tsangaris, C. Housiadas, Appl. Math. Modell. 37 (2013) 5591.
[6] L.T. Choi, J.Y. Tu, H.F. Li, F. Thien, Inhalation Toxicol. 19 (2007) 117.
[7] A. Farkas, I. Balashazy, Comput. Biol. Med. 38 (2008) 508.
[8] P.W. Longest, S. Vinchurkar, J. Biomech. 40 (2007) 305.
[9] J.K. Comer, C. Kleinstreuer, Z. Zhang, J. Fluid Mech. 435 (2001) 25.
[10] Z. Zhang, C. Kleinstreuer, C.S. Kim, Int. J. Multiphase Flow 28 (2002) 1021.
[11] C.L. Lin, M.H. Tawhai, E.A. Hoffman, Wiley Interdisciplinary Reviews-Systems Biology and Medicine, 5, 2013, pp. 643.
[12] N. Nowak, P.P. Kakade, A.V. Annapragada, Ann. Biomed. Eng. 31 (2013) 374.
[13] K.R. Minard, A.P. Kuprat, S. Kabilan, R.E. Jacob, D.R. Einstein, J.P. Carson, R.A. Corley, J. Magn. Reson. 221 (2012) 129.
[14] C.J. Hegedus, I. Balashazy, A. Farkas, Respir. Physiol. Neurobiol. 141 (2004) 99.
[15] L. Gradon, D. Orlicki, J. Aerosol Sci. 21 (1990) 3.
[16] I. Balashazy, W. Hofmann, J. Aerosol Sci. 24 (1993) 745.
[17] T. Heistracher, W. Hofmann, J. Aerosol Sci. 26 (1995) 497.
[18] D. Lee, S.S. Park, G.A. Ban-Weiss, M.V. Fanucchi, C.G. Plopper, A.S. Wexler, Anatomical Record – Adv. Integr. Anatomy Evol. Biol. 291 (2008) 379.
[19] J.R. Hammersley, D.E. Olson, J. Appl. Physiol. 72 (1992) 2402.
[20] J. Zhang, P.C. Johnson, A.S. Popel, Phys. Biol. 4 (2007) 285.
[21] B. Das, G. Enden, A.S. Popel, Ann. Biomed. Eng. 25 (1997) 135.
[22] X. Yin, T. Thomas, J. Zhang, Microvasc. Res. 89 (2013) 47.
[23] Y. Zhang, W.H. Finlay, Aerosol Sci. Technol. 39 (2005) 394.